PCCP

Physical Chemistry Chemical Physics
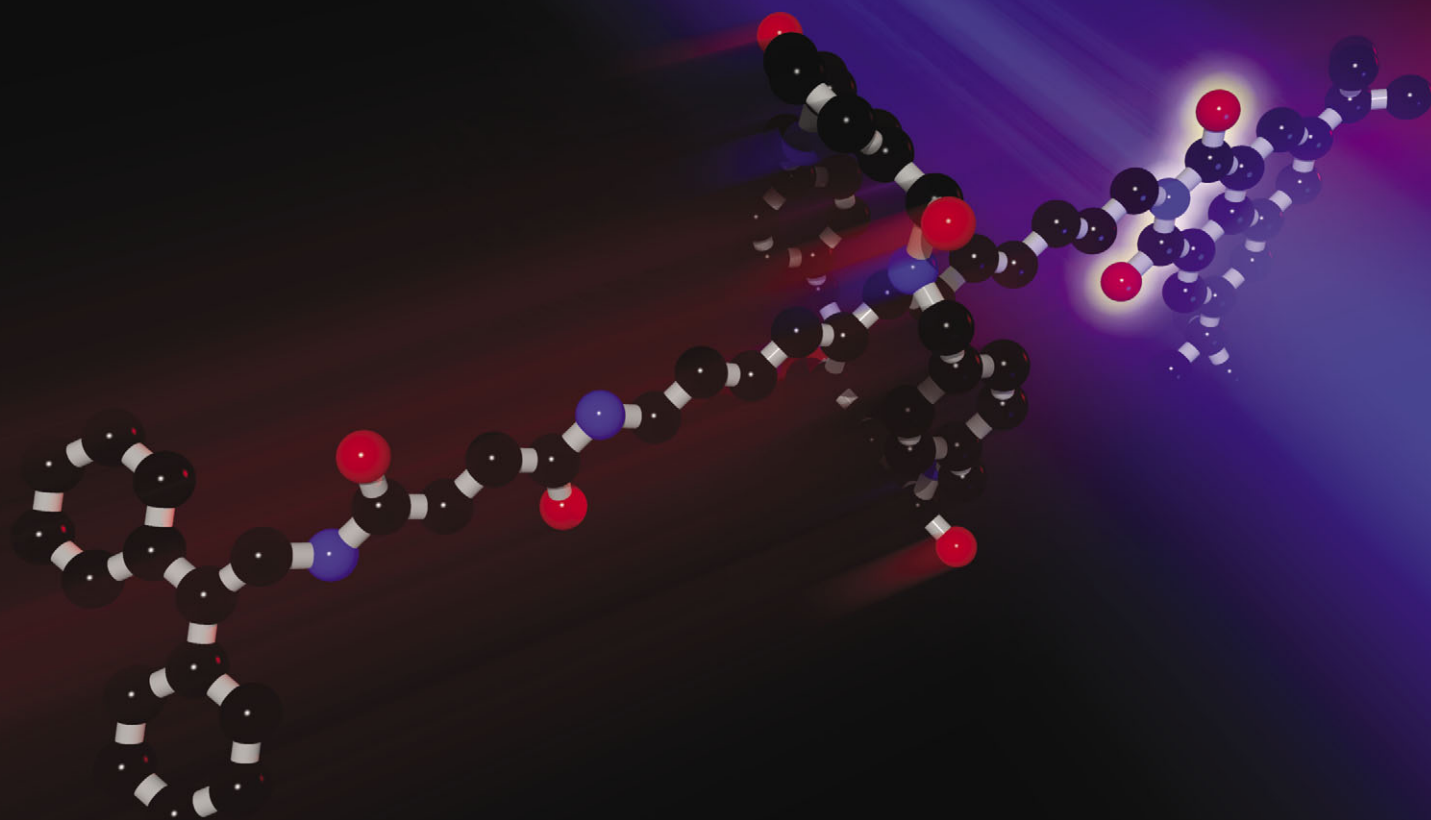
COVER ARTICLE
Woutersen *et al.*
Time-resolved vibrational spectroscopy of a molecular shuttle

Time-resolved vibrational spectroscopy of a molecular shuttle†

Matthijs R. Panman,[a] **Pavol Bodis,**[a] **Danny J. Shaw,**[a] **Bert H. Bakker,**[a]
Arthur C. Newton,[a] **Euan R. Kay,**[b] **David A. Leigh,***[b] **Wybren Jan Buma,***[a]
Albert M. Brouwer*[a] **and Sander Woutersen***[a]

Time-resolved vibrational spectroscopy is used to investigate the inter-component motion of an
ultraviolet-triggered two-station molecular shuttle. The operation cycle of this molecular shuttle
involves several intermediate species, which are observable in the amide I and amide II regions of
the mid-IR spectrum. Using *ab initio* calculations on specific parts of the rotaxane, and by
comparing the transient spectra of the normal rotaxane with that of the *N*-deuterated version,
we can assign the observed vibrational modes of each species occurring during the shuttling cycle in
an unambiguous way. The complete time- and frequency-dependent data set is analyzed using
singular value decomposition (SVD). Using a kinetic model to describe the time-dependent
concentrations of the transient species, we derive the absorption spectra associated with each stage
in the operation cycle of the molecular shuttle, including the recombination of the charged species.

1 Introduction

Recent developments in supramolecular chemistry have led
to the synthesis of a multitude of molecular devices capable
of mimicking the function of macroscopic machinery. They
include molecular shuttles,[2–4] propellers,[5] gears,[6] ratchets,[7]
valves,[8] turnstiles,[9] motors,[10–13] brakes,[14] and elevators.[15] Indu-
cing and controlling the motion of such devices is of fundamental
interest if these devices are to be used as a basis for the construc-
tion of more complex and useful molecular machines. However,
the analogy between molecular devices and their macroscopic
counterparts, appealing as it may be, does not hold at a molecular
level. Macroscopic concepts such as viscous friction lose meaning
as the size and speed of motion of the device approach that of
solvent molecules.[16–19] Also, random thermal motion, both of
the surrounding solvent molecules and of the components of the
molecular machines themselves, will inevitably lead to a certain
degree of unpredictability in the device's motion.

Observing the underlying elementary events of the motion
of molecular machines requires a technique with high struc-
tural sensitivity as well as sufficient time resolution. Most
spectroscopic methods that have been used previously to
investigate molecular machines (X-ray reflectometry,[20] circular
dichroism,[11] steady-state absorption spectroscopy,[21–25] cyclic
voltammetry,[8,15,21] and NMR[26]) do not provide sufficient time
resolution to observe the devices in operation. Transient
UV-VIS spectroscopy[2] has the required time resolution, but
probes the conformation in an indirect manner. Time-resolved
vibrational spectroscopy is an experimental method which pro-
vides both structural sensitivity and temporal resolution.[27–30] In
particular, the possibility to probe the stretching modes of
specific, localized, chemical bonds allows for a direct view on
conformational changes at the molecular level, making it possible
to probe the individual components of a molecular machine and
their interactions in a direct manner. The time resolution of the
probing is determined by the duration of the IR-probe pulse, and
can in principle be as short as 100 fs.[31]

We have demonstrated recently how time-resolved UV-pump
IR-probe experiments can be used to unravel the operation
mechanism of rotaxane-based molecular shuttles.[32] Here, we report
more extensive UV-IR experiments, in which we investigate a
larger range of both IR-probe frequencies and time delays. We
confirm our assignments using *ab initio* calculations on (parts of)
the rotaxane in each stage of the operation cycle. We also perform
a detailed analysis of the kinetics using singular value decomposi-
tion (SVD). In this way, we determine the number of significant
spectral and temporal components in the data in an objective
manner.[33,34] From the SVD, we reconstruct the vibrational spec-
trum of the rotaxane shuttle in each stage of its operation cycle.

[a] *Van't Hoff Insitute for Molecular Sciences, University of
Amsterdam, Science Park 904, 1098 XH Amsterdam,
The Netherlands. E-mail: w.j.buma@uva.nl, a.m.brouwer@uva.nl,
s.woutersen@uva.nl; Fax: +31 20 525 5963; Tel: +31 20 525 7091*
[b] *University of Edinburgh, School of Chemistry, King's Buildings,
West Mains Road, Edinburgh EH9 3JJ, UK.
E-mail: david.leigh@ed.ac.uk*
† Electronic supplementary information (ESI) available: Cross-corre-
lation of the UV pump pulse with the mid-IR probe pulse (Fig. S1);
structures of the model systems used for the calculations of the
vibrations (Fig. S2); plot of the weights of the principal components
obtained from the SVD (Fig. S3); plots of the first four target and
projection vectors obtained from the SVD (Fig. S4); the Mathematica[1]
code for the numerical integration of the kinetic differential equations
and their proposed solutions. See DOI: 10.1039/c1cp22146a

This journal is © the Owner Societies 2012

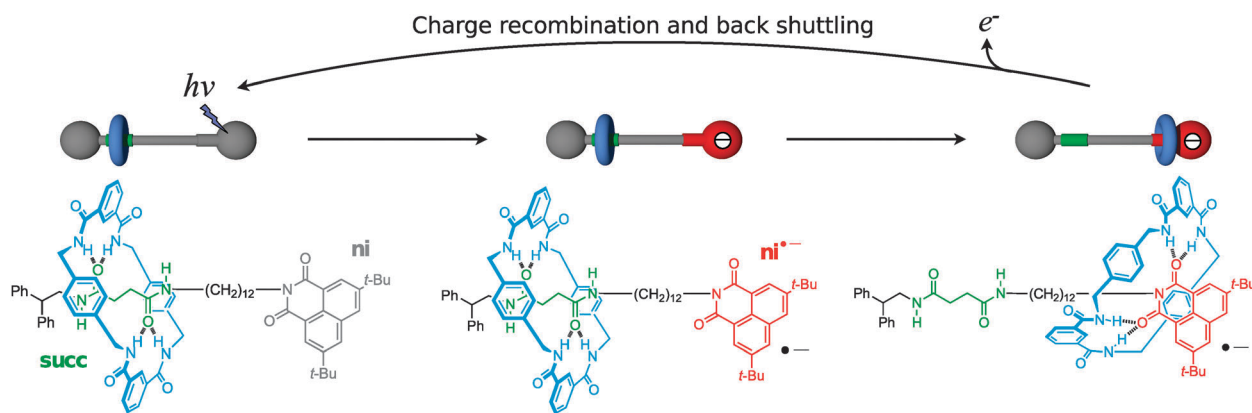*Phys. Chem. Chem. Phys.*, 2012, **14**, 1865–1875 | 1865

Fig. 1 Chemical structures of the [2]rotaxane shuttle in the neutral, initial radical-anion and final radical-anion states. 1,4-Diazabicyclo[2.2.2]octane was used as external electron donor.

Rotaxanes are compounds that consist of a macrocycle that is mechanically interlocked onto a linear thread.[35] The structure of the rotaxane-based molecular shuttle studied here is shown in Fig. 1. There are two specific positions (stations) on the thread at which the macrocycle (blue in Fig. 1) can form hydrogen bonds. These hydrogen bonds are formed between the NH groups of the macrocycle and the CO groups of the thread. The naphthalimide station (**ni**, grey in Fig. 1) is a poor hydrogen-bond acceptor in its electronic ground state.[36] Therefore, in the neutral rotaxane, the ring resides predominantly ($>99\%$) on the succinamide station (**succ**, green in Fig. 1). The macrocycle can be induced to move from the **succ** to the **ni** station by means of an electrochemical or photochemical reduction of the **ni** station. In the latter case, excitation of the naphthalimide station with a 355 nm pulse results in rapid ($\tau = 1.6$ ns) intersystem crossing to the triplet state.[37] In this state, the **ni** station can be reduced by an external electron donor to form a radical anion. In the radical anion state, the naphthalimide station (**ni•⁻**, red in Fig. 1) has a much higher hydrogen-bonding affinity towards the macrocycle than the **succ** station (equilibrium constant > 1000).[3] As a consequence, the macrocycle moves over the thread and forms hydrogen bonds with the **ni•⁻** station. This process occurs on a time scale of 1 μs. Subsequently, slow (~ 100 μs) charge recombination between the **ni•⁻** station and radical cation of the electron donor occurs. This is accompanied by back-shuttling of the macrocycle. After reformation of the hydrogen bonds between the macrocycle and the **succ** station, the system is ready to shuttle again.[2] In the time-resolved experiments we trigger the translation of the macrocycle with a short UV pulse, and observe the subsequent vibrational absorption change using a delayed mid-IR probe pulse. By recording data at different time delays of the probe pulse with respect to the pump pulse, we measure the time dependence of the absorption changes of the molecular device.

2 Experiment

2.1 Ultraviolet-pump infrared-probe setup

For the UV-IR pump-probe experiments we use a commercial Ti:sapphire laser (Spectra-Physics Hurricane, 800 μJ, 100 fs FWHM) synchronised with a commercial, pulsed Nd:YAG laser of which we use the third harmonic (IB Laser DiNY pQ, 355 nm, 0.58 mJ, 3 ns). A variable, computer-controlled time delay between the two laser outputs is achieved in a similar manner as reported by other groups,[38,39] using an electronic configuration as shown in Fig. 2. A residual output from the Ti:sapphire oscillator (80 MHz) is detected by a fast photodiode, amplified and frequency-divided to produce a 1 kHz signal. This signal triggers (1) a pulse generator which provides the triggering for the YLF pump laser and Pockels-cell driver of the regenerative amplifier, (2) an electronically gated amplifier used to record the signals of the MCT-detector array and (3) a computer-controlled electronic delay generator (Berkeley Nucleonics Corporation Model 575-4C). The latter provides the triggering for the Nd:YAG laser that generates the UV pump pulse. The maximum delay between the UV and mid-IR laser pulses is determined by the repetition rate of the Ti:sapphire laser.

The 355 nm pulse length is determined from a cross-correlation with the mid-IR pulses obtained by differentiating the pump–probe signal in a Ge plate. From a fit to a gaussian function we obtain a full-width half-maximum (FWHM) of 3.6 ± 0.4 ns for the pump pulse. The Nd:YAG laser is pumped at 500 Hz and Q-switched at 50 Hz. Using the amplified 800 nm output of the Hurricane and an optical setup described elsewhere[40] we obtain mid-IR pulses with a duration of ~ 150 fs, a bandwidth of 200 cm^{-1} and an energy of 1 μJ. Probe and reference pulses are obtained from the mid-IR light by reflection off the front and back surfaces of a wedged BaF$_2$ window. The UV-IR pump–probe experiment is performed by focusing the 355 nm output several cm behind the sample with an $f = 200$ mm lens. The changes induced in the sample are monitored by the mid-IR probe pulses, which are spatially overlapped with the pump beam, at various time delays between the UV-pump and mid-IR probe pulse. The mid-IR reference beam passes through an area of the sample not influenced by the pump. Both probe and reference beams are focused through the sample by means of an $f = 100$ mm off-axis parabolic mirror. At the sample, the UV and mid-IR beam diameters are 1 mm and 200 μm, respectively. The polarisation of the UV-pump and mid-IR probe are perpendicular with respect to one another. Transient absorption changes are measured by frequency-dispersed detection of the mid-IR pulses using a
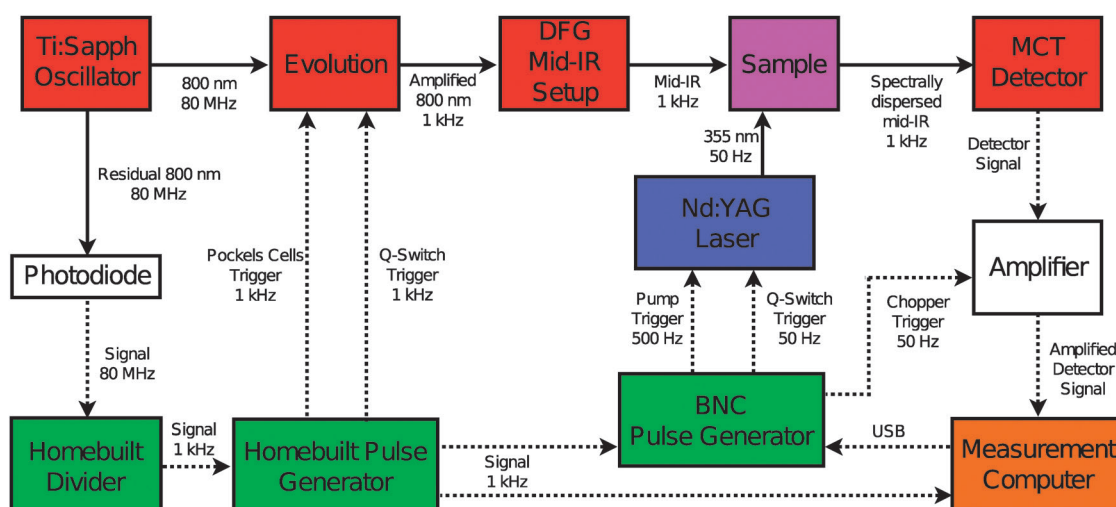
Fig. 2 Electronic setup used to synchronise the Ti:sapphire and Nd:YAG laser systems. The solid lines represent light pulses, the dashed lines represent electronic pulses. The different colors indicate: electronics (green); infrared source and detection (red); UV source (blue); sample (purple); light and signal amplification (white); data acquisition (orange).

2×32 HgCdTe (MCT) array detector (Infrared Associates). Four consecutive measurements with different center frequencies of the IR probe pulse are necessary to construct the UV-IR transient spectra shown in the main text. From the overlapping spectral regions, we find that no scaling of the data of different spectral windows is required. In the case of overlapping frequencies, the pixels with the best signal-to-noise were used. All steady-state Fourier-transform infrared (FTIR) spectra are measured on a Bruker Vertex 70 spectrometer (resolution 2 cm^{-1}). All rotaxane experiments are carried out on a solution of the rotaxane (10^{-4} M) and 1,4-diazabicyclo[2.2.2]-octane (DABCO, 10^{-2} M) in CD$_3$CN (Eurisotop, $>99.8\%$ D purity). Neither the solvent nor DABCO has absorption bands in the spectral region of interest. Argon is bubbled through the sample for 15 min in order to remove dissolved oxygen from the solution. The sample is kept in a sealed IR cell consisting of two CaF$_2$ windows separated by a 10 mm spacer. The experiments are conducted at room temperature (21 °C).

Model calculations of the vibrational spectra in the harmonic approximation were performed on fragments of the actual rotaxanes with Gaussian09, rev. A02.[41] Structures of the fragments are shown in the ESI.† For most calculations, the B3LYP hybrid functional with the 6-31G(d) basis set was used. Test calculations did not show significantly improved agreement with experiment when the 6-31+G(d) or the 6-311G(d,p) basis sets were applied. A common scaling factor of 0.973 was derived for the vibrational frequencies of all fragments by fitting them to the experimental frequencies (Table 1). The bands of the triplet state and the amide II vibrations were not used in the scaling. The scaling factor agrees well with that published by Scott and Radom.[42]

3 Results and discussion

The remainder of the article is organized as follows. We begin by discussing the steady-state IR spectra of the rotaxane and thread. After that, the transient spectra of the rotaxane as it progresses through the shuttling cycle (triplet, radical anion before shuttling, and radical anion after shuttling) are discussed.

The numbering of the peaks in all spectra corresponds to that used in Table 1. The color-coding of the labels corresponds with that used for the different components of the rotaxane in Fig. 1. The complete transient spectral data are then analyzed using singular-value decomposition. By combining this analysis with a quantitative model for the kinetics, we derive the species-associated spectra of the triplet, initial radical-anion and final radical-anion states of the rotaxane and thread.

3.1 Steady-state infrared spectrum

Fig. 3 shows the steady-state Fourier transform infrared (FTIR) spectra of the thread and rotaxane. The peaks in the rotaxane FTIR spectrum can be assigned by comparison with spectra of the constituent components,[25] and using the results of the *ab initio* calculations (see ESI†). We begin by describing the infrared spectrum of the thread. The symmetric and antisymmetric CO-stretch modes of the **ni** station are observed at 1701 cm^{-1} (peak 1) and 1662 cm^{-1} (peak 2), respectively. The absorption band at 1662 cm^{-1} has a broad, high-frequency shoulder (1678 cm^{-1}) belonging to CO-stretch vibrations of the **succ** station (peak 16). An aromatic ring vibration (peak 4) absorbs at 1633 cm^{-1}. The peaks at 1605 cm^{-1} and 1580 cm^{-1} (peaks 6 and 7) are assigned to aromatic ring vibrations of the **ni** unit, as well. The broad band (peak 8), peaking at 1540 cm^{-1}, is the amide II (mainly NH-bending) vibration of the **succ** station.

The differences between the thread and rotaxane spectra are caused by the hydrogen-bonding interaction between macrocycle and thread. These differences are most clearly observed at 1662 cm^{-1}. Compared to the thread, the **succ** CO-stretch band in the rotaxane has redshifted because the CO groups of the **succ** station are hydrogen bonded to the macrocycle. The redshifted CO-stretch mode of the **succ** station appears as peak 5, which overlaps with peak 4 at 1633 cm^{-1}. The absorption spectrum of the rotaxane also contains a contribution from the CO-stretch vibration of the macrocycle (peak 3). The final difference between the spectra of thread and rotaxane is that the amide II band in the latter contains an additional contribution from the macrocycle (peak 9). On the low-frequency side NH

Table 1 Overview of the vibrational modes with their corresponding frequencies and description of the molecular shuttle in the ground, triplet and radical-anion state. "Ar" stands for aromatic ring vibration; "Rad. anion" for radical anion

Peak number	Mode	Experimental frequency/cm^{-1}	Calculated and scaled frequency/cm^{-1}	Hydrogen-bonded	Nature of vibration	Electronic state of naphthalimide
1	$\mathbf{ni_s}$	1700	1703[a]	No	Imide	Ground
2	$\mathbf{ni_{as}}$	1663	1660[a]	No	Imide	Ground
3	$\mathbf{mc}$	1663	1664–1673[b]	No	Amide I	Ground
4	$\mathbf{ni_{Ar}}$	1632	1627[a]	No	Ar	Ground
5	$\mathbf{succ}$	1632	1627[b]	Yes	Amide I	Ground
6	$\mathbf{ni_{Ar}}$	1603	1596[a]	No	Ar	Ground
7	$\mathbf{ni_{Ar}}$	1580	1569[a]	No	Ar	Ground
8	$\mathbf{succ_{NH}}$	1530	1538–1554[b]	Yes	Amide II	Ground
9	$\mathbf{mc_{NH}}$	1530	1538–1554[b]	Yes	Amide II	Ground
10	$\mathbf{ni_s}$	1632	1629[aT]	No	Imide	Triplet
11	$\mathbf{ni_{as}}$	1591	1584[aT]	No	Imide	Triplet
12	$\mathbf{ni_s^{\bullet-}}$	1613	1623[a•−]	No	Imide	Rad. anion
13	$\mathbf{ni_{Ar}^{\bullet-}}$	1565	1571[a•−]	No	Imide	Rad. anion
14	$\mathbf{ni_{Ar+as}^{\bullet-}}$	1531	1537[a•−]	No	Imide	Rad. anion
15	$\mathbf{ni_{as+Ar}^{\bullet-}}$	1531	1537[a•−]	No	Ar	Rad. anion
16	$\mathbf{succ}$	1678	1689[d]	No	Amide I	Rad. anion
17	$\mathbf{mc}$	1654	1660–1668[c]	No	Amide I	Rad. anion
18	$\mathbf{ni_s^{\bullet-}}$	1592	1581[c]	Yes	Amide I	Rad. anion
19	$\mathbf{mc_{NH}}$	1555	1554–1561[c]	Yes	Amide II	Rad. anion
20	$\mathbf{ni_{Ar+as}^{\bullet-}}$	1519	1516[a•−]	No	Imide	Rad. anion
21	$\mathbf{ni_{as+Ar}^{\bullet-}}$	1491	1488[c]	Yes	Mixed	Rad. anion

The calculated frequencies were obtained from DFT at the B3LYP/6-31G(d) level on the following model compounds: [a] *n*-Propyl-naphthalimide station; [aT] *n*-propyl-naphthalimide station in the triplet state; [a•−] radical anion *n*-propyl-naphthalimide station. [b] Methyl-succinamide station-macrocycle pseudo-rotaxane. [c] Radical anion *n*-propyl-naphthalimide station-macrocycle pseudo-rotaxane. [d] Methyl-succinamide station. See ESI Fig. S2 for structures of the fragments. Peaks 14 and 15 are indistinguishable in the calculations.
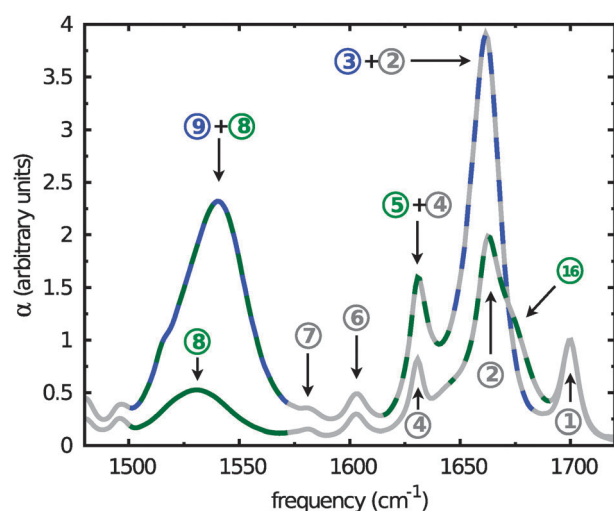

Fig. 3 Normalized solvent-corrected FTIR spectrum of the rotaxane and thread in the range of 1490–1720 cm^{-1}. The numbering corresponds with that used in Table 1. The colors of the labels correspond to those of the components of the rotaxane shown in Fig. 1.

groups contribute that are less involved in hydrogen bonding (those of the thread), the high-frequency amide II vibrations are from hydrogen-bonded NH groups (those of the macrocycle).

3.2 Transient ultraviolet-pump infrared-probe spectra

All the transient IR spectra shown in this subsection are normalized on peak 1. The time-dependence of peak 1 is determined only by the recombination of the $\mathbf{ni^{\bullet-}}$ station with DABCO$^{\bullet+}$. By the normalization we remove this contribution from the signal and

are left with spectral changes caused by radical-anion creation and shuttling. This makes for an easier qualitative discussion of the spectra. The recombination of the charged species is treated in Section 3.3.

3.2.1 Triplet state. The first observable species in the UV-IR shuttling experiment is the triplet state of the **ni** station. This state is difficult to observe separately in the shuttling experiments, because in the presence of the external electron donor, it is rapidly converted into a radical anion (on a time scale of approximately 30 ns). We can measure the pure triplet state spectrum by exciting the rotaxane in the absence of the external electron donor. This measurement also serves as a check to confirm that the frequency shifts observed in the presence of an electron donor (Section 3) are indeed caused by reduction of the **ni** station. The normalized UV-IR transient spectra of the rotaxane in the absence of the electron donor are shown in Fig. 4.

The negative peaks 1 and 2 are the ground-state bleaching of the **ni** symmetric and antisymmetric CO-stretch modes. This bleaching is caused by the transfer of rotaxane population from the electronic ground state to the triplet state. The absorptions of the symmetric and antisymmetric CO-stretch vibrations in the triplet state are visible at 1632 cm^{-1} and 1592 cm^{-1} (peaks 10 and 11). In the delay range probed in Fig. 4, there are no time-dependent changes in the intensities of the peaks other than the relaxation of the triplet state to the electronic ground state which occurs with a lifetime of 44 μs.[43] The lack of dynamics other than the relaxation of the triplet state to the ground state suggests that no shuttling occurs in the triplet state.
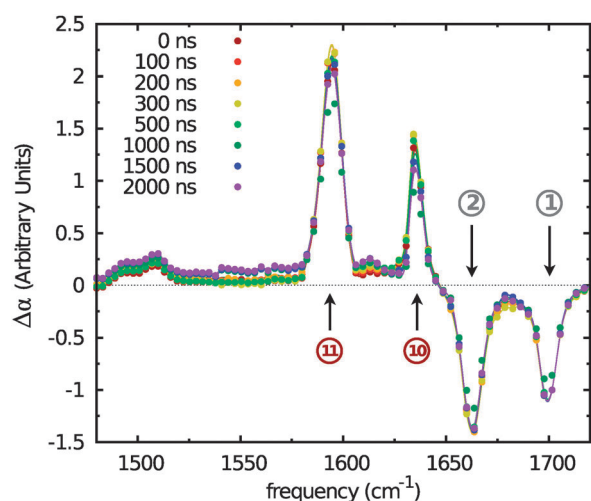
Fig. 4 Normalized UV-IR spectra of the rotaxane in the absence of an external electron donor at several delays after UV excitation. The curves are a guide to the eye. The numbering corresponds with that used in Table 1. The colors of the labels correspond to those of the components of the rotaxane shown in Fig. 1.

3.2.2 Radical anion before shuttling. The reduction of the **ni** station in the triplet state to generate a radical anion is the next step of the operating cycle. As in the case of the triplet state, the radical anion species before shuttling cannot be observed separately in the time-resolved shuttling experiment. This is because significant contributions from both triplet and final (post-shuttling) radical-anion species are always present together with the initial (pre-shuttling) radical-anion state (see Section 3.3). This problem can be solved by exciting the thread (instead of the rotaxane) in the presence of the external electron donor. The normalized UV-IR transient spectra of the thread in the presence of an electron donor are shown in Fig. 5.

At short delays, we observe the spectrum of the thread in the triplet state. This closely resembles the spectrum of the rotaxane
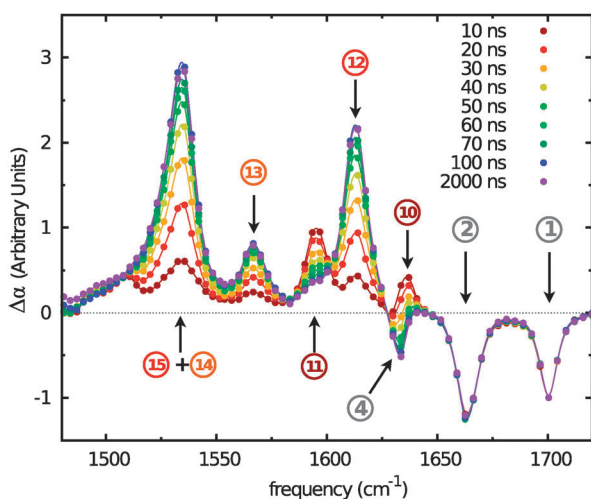

Fig. 5 Normalized UV-IR spectra of the thread in the presence of an external electron donor at different delays. The curves are a guide to the eye. The numbering corresponds with that used in Table 1. The colors of the labels correspond to those of the components of the rotaxane shown in Fig. 1.

in the absence of the external electron donor, see Fig. 4. This means that at short delays the presence or absence of the macrocycle has no influence on the transient spectrum, confirming that the spectral changes are due to changes in the naphthalimide moiety of the thread only. At delays > 100 ns we observe the spectrum of the radical-anion form of the thread, generated by electron transfer from DABCO to the **ni** in the triplet state. A new negative signal becomes visible at 1633 cm^{-1} (peak 4). This is because the aryl ring vibration of the naphthalimide anion is shifted to a lower frequency with respect to the neutral species. The calculations indicate that in the anion some mixing of this aryl mode with the antisymmetric imide stretch occurs. The absorption of this mode is peak 13. The broad and intense peak found at 1531 cm^{-1} is another combination of the radical-anion state antisymmetric CO-stretch vibration (peak 15) and an aromatic ring vibration of the **ni**$^{•-}$. The ground-state bleaching of the latter is probably hidden under the low-frequency side of peak 12. The assignments of peaks 14 and 15 are based on arguments made in Section 3. In the thread no shuttling occurs, so there is no further evolution of the spectrum other than the overall decrease in signal due to charge recombination.

3.2.3 Radical anion after shuttling. The final step in the operating cycle of the rotaxane is the formation of the final radical-anion species in which the macrocycle has broken free from the **succ** station, shuttled over the thread, and formed new hydrogen bonds with the **ni**$^{•-}$ station (see Fig. 2). The spectral changes between the post-shuttling and the initial radical-anion state involve the breaking of the hydrogen bonds between the **succ** station and the macrocycle, and the formation of hydrogen bonds between the macrocycle and the **ni**$^{•-}$ station. Normalised UV-IR transient spectra at several delays after UV excitation of the rotaxane in the spectral range 1480–1720 cm^{-1} are shown in Fig. 6.

The transient spectrum of the rotaxane at 100 ns (Fig. 6) matches that of the reduced thread (Fig. 5) at delays ≥ 100 ns. The changes observed after 100 ns in the rotaxane spectrum can therefore be attributed to the departure of the macrocycle from the **succ** station and its arrival at the **ni**$^{•-}$ station. This motion is possible due to the breaking and making of hydrogen bonds between the different components of the rotaxane involved in the shuttling. In the case of CO-stretch vibrations for this type of system, the red-shift in frequency caused by hydrogen bonding compared to the free (non-hydrogen bonded) situation is typically 20–40 cm^{-1}.[44,45] This frequency shift is accompanied by a broadening due to a distribution of possible hydrogen-bond strengths. In contrast to the CO-stretch mode, the NH-bend mode of a hydrogen bonded NH group is blue-shifted compared to that of a free NH group.[44,45] The hydrogen bonding increases the restoring force of the bending mode, thereby increasing its frequency. The calculations show frequency differences of the amide II modes of up to 30 cm^{-1}, which span the width of the observed amide II band.

The first step in the shuttling process involves the breaking of the hydrogen bonds between the macrocycle and the **succ** station.[32] This is observed as a decrease in absorption of the hydrogen-bonded CO-stretch vibration (peak 5) as delay increases. The complementary, non-hydrogen bonded CO-stretch vibration
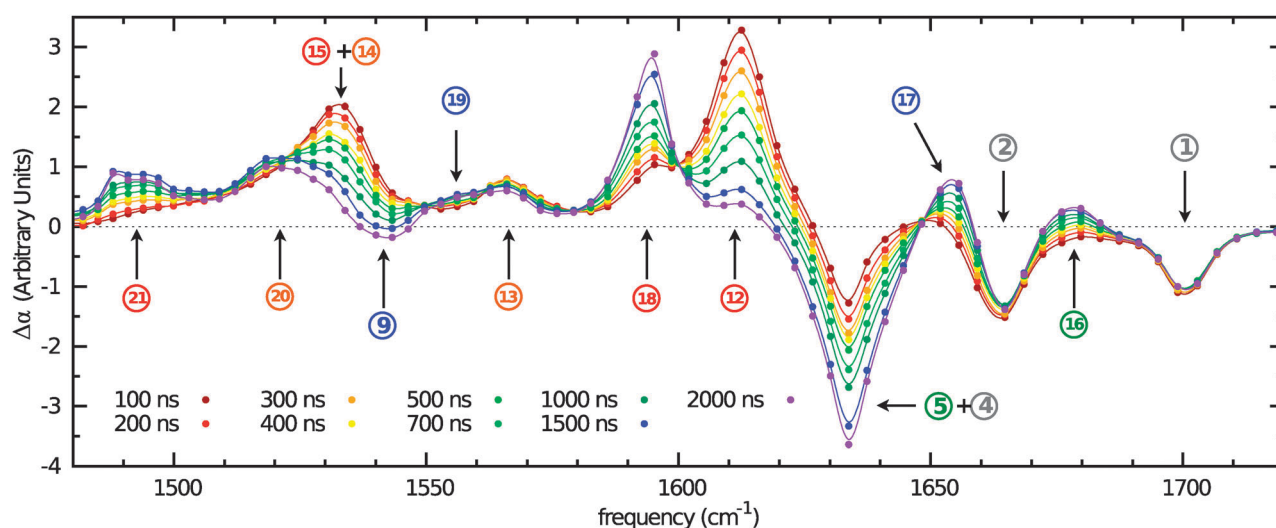
Fig. 6 Normalized UV-IR spectrum of the rotaxane in the spectral region of 1475–1720 cm^{-1}. The curves are a guide to the eye. The numbering corresponds with that used in Table 1. The colors of the labels correspond to those of the components of the rotaxane shown in Fig. 1.

of the **succ** station (peak 16) is observed at 1679 cm^{-1}. The **succ** station CO-stretch frequency (peak 16) in the final state is blue-shifted compared to that in the initial state (peak 5) due to the lack of hydrogen bonding with the macrocycle. The opposite happens for the **ni**$^{\bullet-}$ station. In the initial state, peak 12 is free from hydrogen bonding. As time progresses, more macrocycle binds to the **ni**$^{\bullet-}$ station and the intensity of this peak decreases. The complementary, hydrogen bonded symmetric CO-stretch (peak 18) is observed at 1591 cm^{-1}. Peak 18 is red-shifted compared to peak 12. This change is a direct consequence of the hydrogen bonding with the macrocycle. Peak 17 is the CO-stretch vibration of the macrocycle when it is bound to the **ni**$^{\bullet-}$ station. The corresponding ground-state bleaching (peak 3) is probably located under peak 2. The 9 cm^{-1} red shift arises because the macrocycle NH groups hydrogen-bond more strongly to the **ni**$^{\bullet-}$ station than to the **succ** station. All the CO-stretches in the rotaxane are amide I (or imide I) vibrations; they contain NH-bend character. Thus, even though the CO-groups of the macrocycle are not directly involved in the hydrogen-bond interaction, they still experience the stronger hydrogen bonding to the **ni**$^{\bullet-}$ station.[25] The DFT calculations predict a red shift of about 5 cm^{-1}, in good agreement with experiment.

The spectrum below 1580 cm^{-1} is rather congested which complicates the assignment of the peaks. However, the situation becomes more straightforward when the NH groups of the rotaxane are deuterated. All contributions from the amide II vibrations are shifted to lower frequencies, well outside our observed spectral range (see Fig. 7 top panel for the FTIR spectrum of the deuterated rotaxane). This allows us to assign the amide II modes in an unambiguous manner. A comparison between the UV-IR spectra of the normal and N-deuterated rotaxane is shown in Fig. 7.

There is no difference between the transient IR spectra of the normal and deuterated rotaxane at 100 ns because there are no changes involving the amide II band between the ground- and the initial radical-anion state. Peak 9 blue-shifts upon shuttling, giving rise to a negative feature at 1540 cm^{-1}
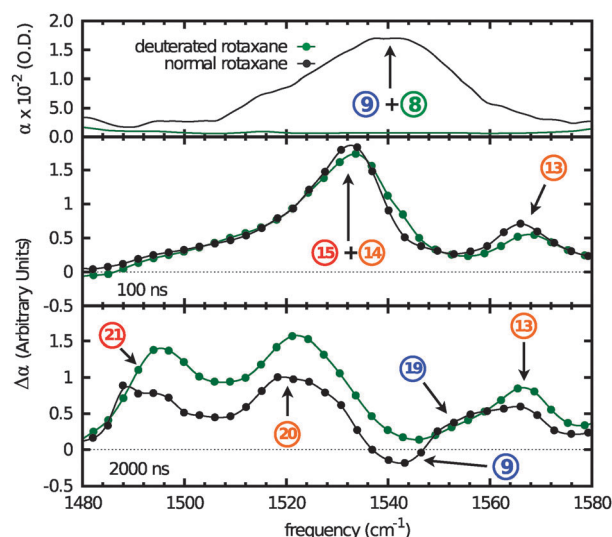

Fig. 7 Top panel: FTIR of the normal and N-deuterated rotaxane in the amide II spectral region. Center panel: normalized initial radical-anion spectra of the normal and N-deuterated rotaxanes at 100 ns after UV-excitation. Bottom panel: normalized final radical-anion spectra of the normal and N-deuterated rotaxane at 2 μs after UV-excitation. The curves are a guide to the eye. The numbering corresponds with that used in Table 1.

and a positive feature at 1555 cm^{-1} (peak 19). Both features disappear after N-deuteration, indicating they belong to an amide II mode. The shift to higher frequencies is evidence of increased hydrogen-bonding strength. This would be the case in the NH groups of the macrocycle. We observe that peak 13 does not change in position or intensity in the deuterated rotaxane. The shuttling of the macrocycle does not affect this peak, which indicates that it most likely belongs to an aromatic ring vibration of the **ni**$^{\bullet-}$ station. The broad, asymmetric absorption peaking at 1531 cm^{-1} at 100 ns remains after deuteration. As time progresses, it decreases in intensity and undergoes a shift towards lower frequencies. A broad peak

at 1491 cm^{-1} (peak 21) increases in intensity with increasing delay. It is clear that the peak at 1531 cm^{-1} originates from several overlapping bands. The calculations (see ESI†) shed light on the nature of these absorptions: in the neutral imide, the symmetric (peak 1) and antisymmetric CO-stretching vibrations (peak 12) are clearly separated from the aromatic ring vibrations (peaks 4, 6, and 7). In the radical anion, however, the frequencies of these modes approach each other. In particular the antisymmetric CO-stretch mode (peak 15) shifts to lower frequencies and as a result mixes with an aromatic ring vibration (peak 14). In the radical anion after shuttling, a further frequency lowering leads to the mixing of the aromatic ring modes with the highest-frequency deformation mode of the *tert*-butyl groups. This results in a strong absorption at 1491 cm^{-1} (peak 21), which has no equivalent in the neutral imide or in the radical anion prior to shuttling. This also explains the shift of peak 14 to lower frequencies (peak 20). Since this predominantly aromatic ring vibration contains significant antisymmetric CO-stretch character, it will experience the hydrogen bonding of the macrocycle to the CO groups of the **ni**$^{\bullet-}$ station.

3.3 Shuttling dynamics

3.3.1 General considerations. We observe that the spectral features of each of the components involved with the shuttling (**succ**, **ni**$^{\bullet-}$, and macrocycle) show the same time-dependence.[32] This can only be the case if the shuttling event in a single rotaxane occurs much faster than observed for the ensemble. The complete operation cycle of the rotaxane involves three time components (see Fig. 1): the conversion of the triplet state into the radical anion, shuttling of the macrocycle, and the charge recombination and back-shuttling. This process spans three orders of magnitude in time (see Fig. 8): the radical-anion formation is witnessed primarily within the first 100 ns. This is followed by the shuttling of the macrocycle, which occurs between 100 ns and 1 μs. Charge recombination is an ongoing process throughout the experiment. It is the main contributor to the changes in the signal from 1 μs onwards. To verify this mechanism in an objective manner, we have analysed the data using singular value decomposition.
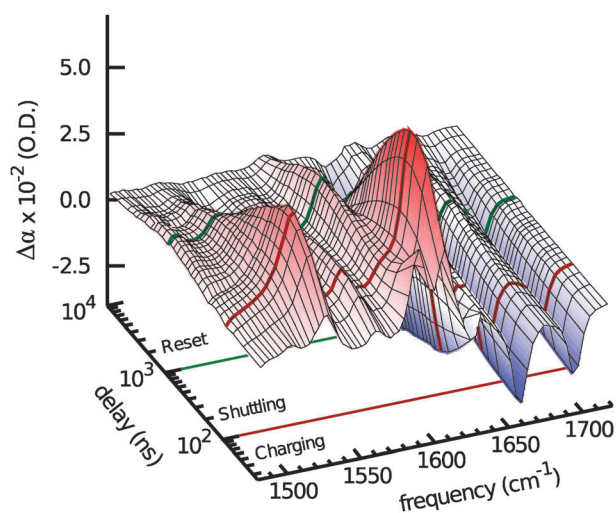

Fig. 8 3-Dimensional representation of the data where change in absorption (Δα) is represented as a function of frequency (cm^{-1}) and time (ns) on a logarithmic scale.

3.3.2 Singular value decomposition. There are two reasons for performing an SVD analysis of our data. The first is that such an analysis can confirm the three-stage shuttling mechanism discussed in the previous section (see also Fig. 1). This mechanism implies that at each time the transient spectrum should be a sum of the spectra of three species (triplet, radical anion before shuttling, radical anion after shuttling), with the contributions of each species depending on time. The second reason is that an SVD makes it possible to obtain the spectra of the rotaxane in each stage of the operation cycle. It is difficult to obtain these spectra directly from the transient measurements, because the shuttling does not occur synchronously for all rotaxane molecules, so that in the transient measurements one always observes a linear combination of the spectra of the individual species. In the previous sections, this problem was partly solved by "freezing" the operation cycle at a specific stage: in particular, we obtained the spectrum of the triplet state by removing the electron donor (so that no reduction occurs), and the spectrum of the pre-shuttling radical-anion state by omitting the macrocycle (so that no shuttling occurs). SVD makes it possible to extract the spectra of the different states in the operation cycle from experimental data obtained with the fully operating molecular device.

The analysis is performed as follows. Our data consist of transient spectra, measured at M frequencies and N delays, with $M > N$. This can be arranged in an $M \times N$ matrix **D** (in our case $M = 77$ and $N = 65$, see Fig. 9 for a graphical representation). This matrix can be decomposed into its principal components using SVD:[33,34,46]

$$\mathbf{D} = \mathbf{U} \cdot \mathbf{\Sigma} \cdot \mathbf{V}^{\mathbf{T}} \qquad (1)$$

$$= \sum_{i=1}^{N} \sigma_i \mathbf{u}_i \mathbf{v}_i^{\mathbf{T}} \qquad (2)$$

where **U** is the $M \times N$ projection matrix, Σ the $N \times N$ diagonal singular-values matrix, and $\mathbf{V}^{\mathbf{T}}$ the $N \times N$ transposed projection matrix. The columns of **U** are the projection vectors $\mathbf{u}_i$ (containing M components), also referred to as the basis spectra of the data. The rows of $\mathbf{V}^{\mathbf{T}}$ are the target vectors $\mathbf{v}_i^{\mathbf{T}}$ (containing N components). The elements of a specific vector $\mathbf{v}_i^{\mathbf{T}}$ represent the delay dependence of the contribution having the corresponding basis spectrum $\mathbf{u}_i$, to the measured data. The data set is thus decomposed into a weighted sum of outer products $\mathbf{u}_i\mathbf{v}_i^{\mathbf{T}}$ of vectors. The singular value σ_i ($i = 1,2,\ldots N$) represents the weight of the ith component of the sum in describing the entire data set.

Often, there is a small subset of weights σ_i that are much larger than all the others. In that case, the experimental data set **D** is very well described by only a limited number $n \ll N$ of basis spectra and corresponding target vectors that have a large weight:

$$\mathbf{D} \approx \sum_{i=1}^{n} \sigma_i \mathbf{u}_i \mathbf{v}_i^{\mathbf{T}} = \tilde{\mathbf{U}} \cdot \tilde{\Sigma} \cdot \tilde{\mathbf{V}}^{\mathbf{T}}, \qquad (3)$$

where $\tilde{\mathbf{U}}$ is the reduced (truncated) $M \times n$ projection matrix, $\tilde{\Sigma}$ the reduced $n \times n$ singular-value matrix, and $\tilde{\mathbf{V}}^{\mathbf{T}}$ the reduced $n \times N$ target matrix. The discarded vectors typically contain noise contributions.

We find that our data can be well described by three vectors ($n = 3$ in eqn (3)). The weights and the first four spectral and target components with the largest singular values are shown
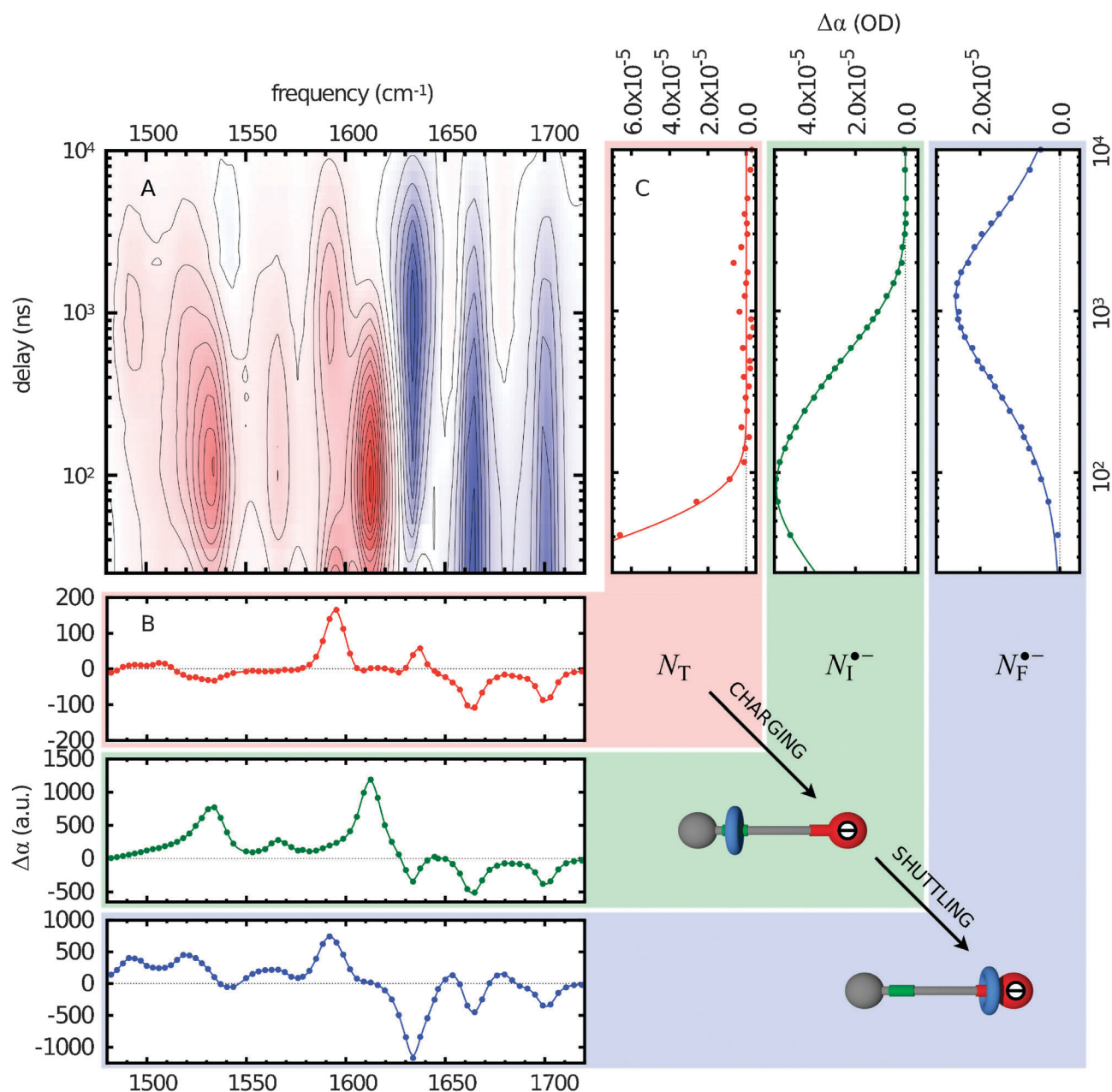
Fig. 9 Singular-value decomposition of the data shown in Fig. 8. (A) 2-Dimensional representation of the data, where blue represents a negative signal and red a positive signal. Species-associated spectra (B) and time-dependence (C). The curves in panel B are guides to the eye. The curves in panel C are the fitted linear combinations of $N_T(t)$, $N_I^{\bullet -}(t)$, and $N_F^{\bullet -}(t)$.

in Fig. S3 and S4 (ESI†). The fourth and higher vectors all represent uncorrelated noise contributions in the signal. This was confirmed by reconstructing the data set from the truncated target, singular-value, and projection matrices. The reconstructed data set ($\tilde{\mathbf{U}} \cdot \tilde{\Sigma} \cdot \tilde{\mathbf{V}}^{T}$ in eqn (3)) can be compared with the original data set (**D** in eqn (3)), taking the uncertainties in the experimental data points into account. The reduced chi-square of the deviations between the reconstructed and the original data obtained in this way is 3.58, which implies that the deviations are on the order of the measurement errors on the data points, and therefore not significant.

The target and projection vectors obtained from an SVD generally cannot be related directly to species-associated spectra

and their corresponding time dependence.[33,46] This is because for any invertible $n \times n$ matrix **C** the decomposition of eqn (3) can be rewritten as

$$\tilde{\mathbf{U}} \cdot \tilde{\Sigma} \cdot \tilde{\mathbf{V}}^{T} = \tilde{\mathbf{U}} \cdot \mathbf{C} \cdot \mathbf{C}^{-1} \cdot \tilde{\Sigma} \cdot \tilde{\mathbf{V}}^{T} \qquad (4)$$

$$= \mathbf{U}_s \cdot \mathbf{V}_s, \qquad (5)$$

where the $M \times n$ matrix $\mathbf{U}_s \equiv \tilde{\mathbf{U}} \cdot \mathbf{C}$ and the $n \times N$ matrix $\mathbf{V}_s \equiv \mathbf{C}^{-1} \cdot \tilde{\Sigma} \cdot \tilde{\mathbf{V}}^{T}$ contain n alternative basis spectra and target vectors, defined by the $n \times n$ transformation matrix **C**, and resulting in exactly the same reconstructed data set. Physically meaningful basis spectra (species-associated spectra) and target vectors (species-associated delay dependencies) can be

obtained from the original SVD components by finding the appropriate transformation matrix $\mathbf{C}$. This is usually done by imposing constraints on the basis spectra and/or target vectors.[34] In particular, by assuming a specific kinetic model to describe the time-dependent species concentrations, it is often possible to determine $\mathbf{C}$, and therefore the species spectra, unambiguously.

To this purpose, we proceed as follows. The transformation $\mathbf{C}$ should be such that $\mathbf{U}_s$ contains the spectra of the three species (triplet, radical anion before shuttling, radical anion after shuttling), and $\mathbf{V}_s$ the time dependencies of their concentrations. The elements of $\mathbf{C}$ are determined by requiring that $\mathbf{V}_s$ has a functional form that represents the time-dependent concentrations of the three species. This is done by assuming a quantitative kinetic model for the delay dependencies of the three species (triplet, radical anion before shuttling, radical anion after shuttling), and optimizing the agreement of $\mathbf{V}_s$ with the predicted time dependencies using a least-squares fit, see the next section.

3.3.3 Kinetic model. Based on the considerations of Section 3.3, the species concentrations are determined by the following set of rate equations:

$$\dot{N}_{T}(t) = -k_{T}N_{T} \tag{6}$$

$$\dot{N}_{I}^{\bullet-}(t) = \eta k_{T}N_{T} - k_{S}N_{I}^{\bullet-} - k_{R}N_{I}^{\bullet-}D^{\bullet+} - k_{Q}N_{I}^{\bullet-} \tag{7}$$

$$\dot{N}_{F}^{\bullet-}(t) = k_{S}N_{I}^{\bullet-} - k_{R}N_{F}^{\bullet-}D^{\bullet+} - k_{Q}N_{F}^{\bullet-} \tag{8}$$

$$D^{\bullet+} = N_{I}^{\bullet-} + N_{F}^{\bullet-}, \tag{9}$$

where $N_{T}(t)$ is the triplet population, k_{T} the pseudo first-order rate constant for the triplet-to-anion conversion (see Section 3), and η the radical-anion yield (some of the population in the triplet state is lost by non-radiative decay, and part of the newly formed radical anion population is rapidly quenched after creation by DABCO$^{\bullet+}$).[37] $N_{I}^{\bullet-}(t)$ is the initial (pre-shuttling) radical-anion population, which has three loss channels. The main loss channels are the shuttling (rate constant k_{S}), and the charge recombination with DABCO$^{\bullet+}$ (second-order rate constant k_{R}). We find that a third, minor loss channel (rate constant k_{Q}) is needed to quantitatively describe the data at long times. This contribution is probably due to quenching of the radical anion by traces of molecular oxygen present in the sample (the resulting superoxide rapidly reacts with DABCO$^{\bullet+}$, so the oxygen concentration remains constant). This loss channel is described by the third term in eqn (7). The third rate equation represents the final (post-shuttling) radical-anion concentration $N_{F}^{\bullet-}(t)$, which has charge recombination and quenching as its only loss channels; finally, $D^{\bullet+}$ is the concentration of DABCO$^{\bullet+}$, which is determined by the requirement of conservation of charge.

Directly upon photo-excitation, intersystem crossing to the triplet occurs (the intersystem crossing can be assumed instantaneous on the time scale of the experiment). We set the initial concentration of triplet species $N_{T} = N_{0}$ (the concentration of triplet generated at $t = 0$) and $N_{I}^{\bullet-}(t) = N_{F}^{\bullet-}(t) = D^{\bullet+} = 0$. As shown in the ESI,† for these initial values, the solutions to rate

eqn (6)–(9) are given to a very good approximation by the following analytical expressions:

$$N_{T}(t) = N_{0}e^{-k_{T}t} \tag{10}$$

$$N_{I}^{\bullet-}(t) = \frac{k_{T}}{k_{T} - k_{S} - k_{Q}} \frac{(e^{-(k_{S}+k_{Q})t} - e^{-k_{T}t})}{\frac{1}{\eta N_{0}} + k_{R}t} \tag{11}$$

$$N_{F}^{\bullet-}(t) = \frac{(e^{-k_{Q}t} - e^{-k_{T}t})k_{T}}{\left(\frac{1}{N_{0}\eta} + k_{R}t\right)(k_{T} - k_{Q})}$$
$$- \frac{(e^{-(k_{Q}+k_{S})t} - e^{-k_{T}t})k_{T}}{\left(\frac{1}{N_{0}\eta} + k_{R}t\right)(k_{T} - k_{Q} - k_{S})} \tag{12}$$

Given a set of rate constants k_{T}, k_{S}, k_{R}, and an initial concentration N_{0}, this set of solutions allows us to predict the species concentrations that should be contained in $\mathbf{V}_s$ as follows:

$$\mathbf{V}_{s}^{calc} = \begin{pmatrix} N_{T}(t_{1}) & N_{T}(t_{2}) & \cdots \\ N_{I}^{\bullet-}(t_{1}) & N_{I}^{\bullet-}(t_{2}) & \cdots \\ N_{F}^{\bullet-}(t_{1}) & N_{F}^{\bullet-}(t_{2}) & \cdots \end{pmatrix}, \tag{13}$$

where t_{i} are the delay values sampled in the time-resolved experiment. From previous UV-Vis measurements it is known that $k_{R} = 9 \times 10^{9} \text{ M}^{-1} \text{ s}^{-1}$ and $\eta = 0.20$.[2,37] Since $\mathbf{C}$ is defined such that $\mathbf{C} \cdot \mathbf{V}_{s} = \tilde{\Sigma} \cdot \tilde{\mathbf{V}}^{T}$ we can determine the unknown elements of $\mathbf{C}$ and the remaining unknown parameters N_{0}, k_{T}, and k_{R} from a global least-squares fit of $\mathbf{C} \cdot \mathbf{V}_{s}^{calc}$ to the matrix $\tilde{\Sigma} \cdot \tilde{\mathbf{V}}^{T}$ as obtained from the SVD. From the resulting least-squares fit, we find $k_{S} = 0.0013 \text{ ns}^{-1}$, $k_{T} = 0.04 \text{ ns}^{-1}$, and $N_{0} = 5.8 \times 10^{-5}$. These values agree well with the ones obtained previously using a smaller data set.[32] Additionally, we find $k_{Q} = 8.8 \times 10^{-5} \text{ ns}^{-1}$.

The species-associated spectra and corresponding time-dependences can now be generated from the resulting $\mathbf{C}$ matrix. They are shown in Fig. 9 (panels B and C, respectively). The species-associated spectra are in good agreement with the spectra obtained by "freezing" the operation cycle: for the triplet spectrum, see Fig. 4; for the pre-shuttling radical anion, see Fig. 5 at delays ≥ 100 ns; for the post-shuttling radical anion, see Fig. 6 at delays ≥ 2 μs. Fig. 9C shows clearly that during the shuttling cycle, most of the time more than one species is present in the sample. In particular, the only species that can be observed in an isolated manner is the radical anion after shuttling, which is the only species present for $t > 5$ μs. As stated before, the advantage of the SVD method is that the species-associated spectra can be determined from the convoluted data set in an unambiguous manner, provided that the kinetic scheme of the dynamic process being studied is known.

4 Conclusion

The work presented here is an extension to the work we published previously on the operation mechanism of a [2]rotaxane.[32] We have extended the range of measured frequencies of the transient IR spectra to lower energies, and comparison of the transient spectra of the normal and N-deuterated rotaxane has enabled us to assign the convoluted peaks observed in the

extended spectral range. The positions and shifts of the peaks are confirmed by DFT calculations performed at the B3LYP/6-31G(d) level. Understanding the assignment and the shifts of the low-frequency range opens up new possibilities for future work. We can study, for example, the shuttling motion of the rotaxane in solvents that are not transparent in the amide I frequency range but are so in the amide II range. Also, since the modes in the amide II frequency range are of a different nature than those in the amide I range, effects involving different functional groups of the rotaxane (in particular NH or CO groups) can be observed separately.

We have used singular value decomposition to obtain the number of species involved in the operation cycle in an objective manner. We applied a kinetic model to the SVD that takes the time-dependence of all three photochemical species into account. In this way we obtained the rates of the different stages of the rotaxane operating cycle as well as the species associated spectra. The SVD allows us to use the entire data set (both the full frequency and the delay ranges) which results in a much more precise determination of the rates involved in the shuttling process than was achieved in our earlier studies. Finally, from the SVD we can determine the spectra of the intermediate species without having to "freeze" the operation cycle of the molecular device.

Acknowledgements

References

1 Wolfram Research, Inc., *Mathematica Edition: Version 6.0*, 2007.
2 A. M. Brouwer, C. Frochot, F. G. Gatti, D. A. Leigh, L. Mottier, F. Paolucci, S. Roffia and G. W. H. Wurpel, *Science*, 2001, **291**, 2124–2128.
3 A. Altieri, F. Gatti, E. R. Kay, D. A. Leigh, D. Martel, F. P. A. M. Slawin and J. K. Wong, *J. Am. Chem. Soc.*, 2003, **125**, 8644–8654.
4 D. D. Gunbas, L. Zalewski and A. M. Brouwer, *Chem. Commun.*, 2010, **46**, 2061–2063.
5 K. Mislow, *Acc. Chem. Res.*, 1976, **9**, 26–33.
6 H. Iwamura and K. Mislow, *Acc. Chem. Res.*, 1988, **21**, 175–182.
7 V. Serreli, C. F. Lee, E. R. Kay and D. A. Leigh, *Nature*, 2007, **445**, 523–527.
8 T. D. Nguyen, Y. Liu, S. Saha, K. C. F. Leung, J. F. Stoddart and J. L. Zink, *J. Am. Chem. Soc.*, 2007, **129**, 626–634.
9 C. Bedard and J. S. Moore, *J. Am. Chem. Soc.*, 1995, **117**, 10662–10671.
10 T. R. Kelly, H. De Silva and R. A. Silva, *J. Am. Chem. Soc.*, 1999, **401**, 150–152.
11 N. Koumura, R. W. J. Zijlstra, R. A. van Delden, N. Harada and B. L. Feringa, *Nature*, 1999, **401**, 152–155.
12 D. A. Leigh, J. K. Y. Wong, F. Dehez and F. Zerbetto, *Nature*, 2003, **424**, 174–179.
13 J. V. Hernández, E. R. Kay and D. A. Leigh, *Science*, 2004, **306**, 1532–1537.
14 T. R. Kelly, M. C. Bowyer, V. Bhaskar, D. Bebbington, A. Garcia, F. Lang, M. H. Kim and M. P. Jette, *J. Am. Chem. Soc.*, 1994, **116**, 3657–3658.
15 J. D. Badjić, V. Balzani, A. Credi, S. Silvi and J. F. Stoddart, *Science*, 2004, **303**, 1845–1849.
16 R. Kubo and N. Hashitsume, *Statistical Physics II: Nonequilibrium Statistical Mechanics*, Springer, Berlin, 1985.
17 R. D. Astumian, *Proc. Natl. Acad. Sci. U. S. A.*, 2005, **102**, 1843–1847.
18 R. D. Astumian, *Phys. Chem. Chem. Phys.*, 2007, **9**, 5067–5083.
19 R. D. Astumian, *Proc. Natl. Acad. Sci. U. S. A.*, 2007, **104**, 19715–19718.
20 K. Nørgaard, B. W. Laursen, S. Nygaard, K. Kjaer, H.-R. Tseng, A. H. Flood, J. F. Stoddart and T. Bjørnholm, *Angew. Chem., Int. Ed.*, 2005, **44**, 7035–7039.
21 S. S. Zhu, P. J. Carrol and T. M. Swager, *J. Am. Chem. Soc.*, 1996, **118**, 8713–8714.
22 S. Garaudée, S. Silvi, M. Venturi, A. Credi, A. H. Flood and J. F. Stoddart, *ChemPhysChem*, 2005, **6**, 2145–2152.
23 D. S. Marlin, D. González Cabrera, D. A. Leigh and A. M. Z. Slawin, *Angew. Chem., Int. Ed.*, 2006, **45**, 77–83.
24 S. Saha, A. H. Flood, J. F. Stoddart, S. Impellizzeri, S. Slivi, M. Venturi and A. Credi, *J. Am. Chem. Soc.*, 2007, **129**, 12159–12171.
25 D. C. Jagesar, F. Hartl, W. J. Buma and A. M. Brouwer, *Chem.–Eur. J.*, 2008, **14**, 1935–1946.
26 F. G. Gatti, S. León, J. K. Y. Wong, G. Bottari, A. Altieri, M. A. F. Morales, S. J. Teat, C. Frochot, D. A. Leigh, A. M. Brouwer and F. Zerbetto, *Proc. Natl. Acad. Sci. U. S. A.*, 2003, **100**, 10–14.
27 K. Kwac and M. Cho, *J. Chem. Phys.*, 2003, **119**, 2247–2255.
28 C. Kolano, J. Helbing, M. Kozinski, W. Sander and P. Hamm, *Nature*, 2006, **444**, 469–472.
29 P. Bodis, M. R. Panman, B. H. Bakker, A. Mateo-Alonso, M. Prato, W. J. Buma, A. M. Brouwer, E. R. Kay, D. A. Leigh and S. Woutersen, *Acc. Chem. Res.*, 2009, **49**, 1462–1469.
30 A. Pfeifer, T. Majerus, K. Zikihara, D. Matsuoka, S. Tokutomi, J. Heberle and T. Kottke, *Biophys. J.*, 2009, **96**, 1462–1470.
31 J. Bredenbeck, J. Helbing, R. Behrendt, C. Renner, L. Moroder, J. Wachtveitl and P. Hamm, *J. Phys. Chem. B*, 2003, **107**, 8654–8660.
32 M. R. Panman, P. Bodis, D. J. Shaw, B. H. Bakker, A. C. Newton, E. R. Kay, D. A. Leigh, A. M. Brouwer, W. J. Buma and S. Woutersen, *Science*, 2010, **328**, 1255–1258.
33 E. R. Henry, *Biophys. J.*, 1997, **72**, 652–673.
34 M. Kubista, J. Nygren, A. Elbergali and R. Sjöback, *Crit. Rev. Anal. Chem.*, 1999, **29**, 1–28.
35 H. L. Frisch and E. Wasserman, *J. Am. Chem. Soc.*, 1961, **83**, 3789–3795.
36 V. Wintgens, P. Valat and J. Kossanyl, *J. Chem. Soc. Faraday Trans.*, 1994, **90**, 411–421.
37 D. C. Jagesar, S. M. Fazio, J. Taybi, E. Eiser, F. G. Gatti, D. A. Leigh and A. M. Brouwer, *Adv. Funct. Mater.*, 2009, **19**, 3440–3449.
38 H. S. Chung, M. Khalil, A. W. Smith and A. Tokmakoff, *Rev. Sci. Instrum.*, 2007, **78**, 063101.
39 C. Krejtschi and K. Hauser, *Eur. Biophys. J.*, 2011, **40**, 673–685.
40 P. Bodis, O. F. A. Larsen and S. Woutersen, *J. Phys. Chem. A*, 2005, **109**, 5303–5306.
41 M. J. Frisch, G. W. Trucks, H. B. Schlegel, G. E. Scuseria, M. A. Robb, J. R. Cheeseman, G. Scalmani, V. Barone, B. Mennucci, G. A. Petersson, H. Nakatsuji, M. Caricato, X. Li, H. P. Hratchian, A. F. Izmaylov, J. Bloino, G. Zheng, J. L. Sonnenberg, M. Hada, M. Ehara, K. Toyota, R. Fukuda, J. Hasegawa, M. Ishida, T. Nakajima, Y. Honda, O. Kitao, H. Nakai, T. Vreven, J. J. A. Montgomery, J. E. Peralta, F. Ogliaro, M. Bearpark, J. J. Heyd, E. Brothers, K. N. Kudin, V. N. Staroverov, R. Kobayashi, J. Normand, K. Raghavachari, A. Rendell, J. C. Burant, S. S. Iyengar, J. Tomasi, M. Cossi, N. Rega, J. M. Millam, M. Klene, J. E. Knox, J. B. Cross, V. Bakken, C. Adamo, J. Jaramillo, R. Gomperts, R. E. Stratmann, O. Yazyev, A. J. Austin, R. Cammi, C. Pomelli, J. W. Ochterski, R. L. Martin,

K. Morokuma, V. G. Zakrzewski, G. A. Voth, P. Salvador, J. J. Dannenberg, S. Dapprich, A. D. Daniels, O. Farkas, J. B. Foresman, J. V. Ortiz, J. Cioslowski and D. J. Fox, *GAUSSIAN 09 (Revision A.02)*, Gaussian Inc., Wallingford, CT, 2009.

42 A. P. Scott and L. Radom, *J. Phys. Chem.*, 1996, **100**, 16502–16513.

43 G. W. H. Wurpel, *PhD thesis*, University of Amsterdam, 2001.

44 W. Reckien, B. Kirchner and S. D. Peyerimhoff, *J. Phys. Chem. A*, 2006, **110**, 12963–12970.

45 A. M. Rijs, I. Compagnon, J. Oomens, J. S. Hannam, D. A. Leigh and W. J. Buma, *J. Am. Chem. Soc.*, 2009, **131**, 2428–2429.

46 W. H. Press, S. A. Teukolsky, W. T. Vetterling and B. P. Flannery, *Numerical Recipes in C*, Cambridge University Press, Cambridge, UK, 1992.

This journal is © the Owner Societies 2012

Phys. Chem. Chem. Phys., 2012, **14**, 1865–1875 | 1875